Combined powder metallurgy routes to improve thermal and mechanical response of Al-Sn composite Phase Change Materials

Chiara Confalonieri[a]*, Maxime Perrin[a], Elisabetta Gariboldi[a]
[a]Politecnico di Milano, Department of Mechanical Engineering, Via La Masa 1, 20156 Milan (Italy)
chiara.confalonieri@polimi.it, maxime.perrin@mail.polimi.it, elisabetta.gariboldi@polimi.it
*corresponding author

Abstract

Powder metallurgy processes are suitable to produce form-stable solid-liquid Phase Change Materials from Miscibility Gap Alloys. In principle, they allow to obtain a composite metallic material with good dispersion of low-melting active phase particles in a high-melting passive matrix, preventing leakage of the first during phase transition and so increasing stability of thermal response. At the same time, the matrix provides structural properties. The aim of this paper is to combine conventional powder mixing techniques (simple mixing and ball milling) to improve both active phase isolation and mechanical properties of an Al-Sn alloy.

Keywords: metallic Phase Change Materials; form-stable; powder metallurgy; thermal stability; mechanical properties; Miscibility Gap Alloys

1. Introduction

Using latent heat Phase Change Materials, thermal energy can be stored and released in the form of latent heat. This potential can be exploited in many different cases of thermal management and research on these materials increased exponentially in the last decades. Using these materials, thermal energy is stored as latent heat during a phase transition and then it is released when the transition is reversed. Usually, the solid-solid and solid-liquid transitions are exploited, thanks to their limited volume expansion with respect to transitions involving gas state [1,2]. Among these two, solid-liquid transitions have higher latent heat, however leakage of molten phase from its container must be prevented [1,2]. In this framework, metallic PCMs are still the less developed class, despite of their high potential for medium- and high-temperature applications (> 120°C) [3,4]. In addition to higher transition and application temperatures, they have also large latent heat per unit volume, high thermal conductivity, good thermal stability and reliability [3,4]. According to Zhou and Wu [4], a common approach to obtain metallic solid-liquid PCMs is encapsulating the PCM in a passive higher-melting material through mechanical processes or electroplating. However, oxidation and degradation at high temperatures can reduce material durability and thermal energy performance; moreover, this process can be complex and expensive [5], as well as thermal conductivity can be too low [1]. A viable alternative is designing a form-stable material, consisting of an active phase (i.e. the actual PCM) embedded in a higher-melting passive matrix. The latter has a double purpose: avoiding leakage of molten active phase and keeping structural properties. To keep microstructural and compositional stability, the two phases must not interact forming intermetallics and solid solutions, since these phenomena reduce the available quantity of active phase. According to Sugo et al. [6], this kind of microstructure can be obtained using Miscibility Gap Alloys (MGAs), i.e. alloys whose phases are immiscible both in liquid and solid state. So, since the solubility of the high-melting matrix in the active phase is low also when the latter is liquid, it is possible to keep a stable composition over time and thermal cycles. Examples of such alloys to be used as PCMs are Al-Sn, Fe-Cu, Fe-Mg and Al-Bi [6]. Among them, previous studies of Authors' research group focused on an Al-Sn alloy [7,8]. The Al-Sn system is a simple eutectic system, but, due to the low solid solubility of the two elements and the eutectic reaction temperature (228°C) close to pure Sn melting temperature (232°C), it can be considered as a metastable MGA [9,10]. The transition temperature of this PCM is assumed almost equal to pure Sn melting temperature and so, according to the PCM classification of Zhou et al. [4], it belongs to the class of medium-temperature PCMs (150÷500°C). The Authors chose this system because, using a simple binary alloy, it is possible to obtain a PCM with transition temperature slightly higher than the maximum temperatures achievable with polymeric PCMs. Further, in addition to its functional properties, this system was selected by the Authors because it had been widely applied in bearing alloys [10–13] and, so, the development of a production process to obtain the same alloy with a completely different application could be based on traditional industrial processes.

A common issue of MGAs is that solidification of casted MGAs results in the high-melting phase surrounded by the lower-melting one [10,11]. Considering Al-Sn systems, this is caused by the significant differences between the two metals in melting temperature, as well as in density [10]. Among the possible solutions, powder metallurgy is a relatively simple and effective technique to obtain the desired structure. This approach has been widely applied to Al-Sn based bearing alloys, in order to obtain a homogenous distribution of Sn particles throughout the component volume [11,12]; as already highlighted, this microstructure is the one desired for PCMs too.

Powder metallurgy process consists of three steps: powder mixing, compression and sintering. Previous studies of Authors' research group [7,8] showed that powder preparation has a strong influence over final properties of an Al-Sn based PCM, which will be considered in this paper too. Testing different compression and heat treatment conditions, Gariboldi and Perrin (2019) [7] focused on simple mixing (SM) of powders, while Confalonieri et al. applied ball milling (BM) [8]. The goal of the latter approach was combining powder mixing to powder size reduction and increase of powder hardness. Preliminary comparison between the two methods [8] showed that, as expected, BM gave a finer microstructure than SM; consequently, also thermal and mechanical response changed. The main advantages and drawbacks for each method are summarized in Table 1 and Table 2.

Simple mixing		
Point of view	**Advantages**	**Drawbacks**
Microstructural	• Good separation of tin particles, especially for cold-pressed materials • Presence of well distinguishable phases (pure Sn & pure Al)	• Coarse microstructure, especially for cold-pressed materials • For hot-pressed materials, sintering heat treatments well above Sn melting temperature lead to the formation of a Sn-rich matrix with embedded Al particles • High porosity after heat treatments
Thermal	• Narrow temperature range of solidification and melting • Well defined melting and solidification peaks	• Low thermal stability due to an easy leakage of tin during sintering heat treatments and service cycles

Table 1. Pros and cons of simple mixing

Ball milling		
Point of view	**Advantages**	**Drawbacks**
Microstructural	• Very fine • No interconnection between Sn particles	• Complex microstructure characterized by three phases • Heat treatments significantly change the microstructure: variation of porosity, change in phase composition and distribution
Thermal	• High thermal stability • Very limited leakage of tin during sintering heat treatments and service cycles	• More extended melting range and extended solidification range • Low value of stored energy

Table 2. Pros and cons of ball milling

The comparison highlighted that the two processes are complementary and, therefore, the conclusion is that an optimized powder preparation based on a combination of ball milling and simple mixing could lead both to a:

- suitable microstructure for metallic composite PCMs (i.e. fine and composed of two phases: Sn particles embedded in Al matrix)
- suitable thermal properties (i.e. high thermal stability and short transition temperature range).

The present paper is focused on the identification of the powder-based production process that could supply the combination of microstructural features and thermal response mentioned above. To determine the best parameters, three new powder mixing methods were developed and applied. The powder blends were then compressed and, in some cases, sintered above Sn melting temperature applying the same process for each sample.

Microstructural, thermal and mechanical characterization was conducted on as-produced samples. The same tests were repeated after thermal cycles simulating service conditions in order to verify thermal stability, i.e. the thermal response does not change during service. Using Al-Sn MGA PCMs, this is strictly connected to the absence of Sn leakage, which reduces the amount of active phase undergoing the transition.

2. Materials and methods

2.1 Powder supply

Samples were produced mixing 20% volume of Sn powders with 80% volume of Al powders, which corresponds to about 40% mass of Sn; from now on alloy compositions in mass fraction will be indicated with m%. The Al powder was an atomized high purity Al (> 99.7 mass%) powder with diameters smaller than 45 μm (ECKA Granules GmbH, Germany). The Sn powder (SN, Metalpolveri S.r.l) was a high purity powder (Sn>99.9% mass), having a very fine particle-size distribution (Over Sieve Grain Size: <25μm 64÷71%, 25μm<OSGS<45μm 20÷26%, 45μm<OSGS<75μm 5÷11%, >75μm <0.3%) and good homogeneity.

2.2 Powder preparation methods

The innovative methods of producing Al-Sn composite PCMs have been designed according to three following basic concepts and observations arising from previously obtained results.

- First, since Al is harder than Sn, Sn particles are significantly deformed when mixed with Al; this results in the formation of Sn aggregates with elongated shapes, instead of the desired round particles.
- Secondly, as already mentioned, ball milling leads to powder-size reduction and hardness increase, with an extent that depends on the process parameters [14]
- Thirdly, simple mixing only blends the powders, without affecting powder size or mechanical properties.

Scheme in Figure 1 summarizes the steps of new powder preparation methods, that will be hereafter referred as Method 1, 2 and 3. In all cases, the first step is ball milling (BM) of Sn powders, with the aim of reducing Sn powder size and increasing particle hardness to reduce the gap with Al. Following this common stage, Method 1 (M1) consists of Simple Mixing (SM) of BM Sn powders: the expected microstructure should contain globular Sn particles. On the other hand, the second step of Method 2 (M2) and Method 3 (M3) involves ball milling of Sn with a part of Al powders, that was aimed at forming an Al or Al-Sn shell around a Sn particle core. Then, in M2, this BM Al-Sn blend is mixed with the rest of unprocessed Al powder; since these are softer than BM powders, their flow between BM powder during compression was expected, leading to very low porosity after compaction and avoiding interconnection between ball-milled particles. Finally, the most complex designed process was M3, in which also the mixture of the last fraction of Al powders was carried out through ball milling. The aim of this process was to form powder particles characterized by a very fine microstructure with graded microstructure with Sn-rich core, that could lead, after compression stage, to a fine dense structure with good isolation of Sn particles. M1 and M3 are supposed to result in completely different microstructures, while M2 should give an intermediate condition.

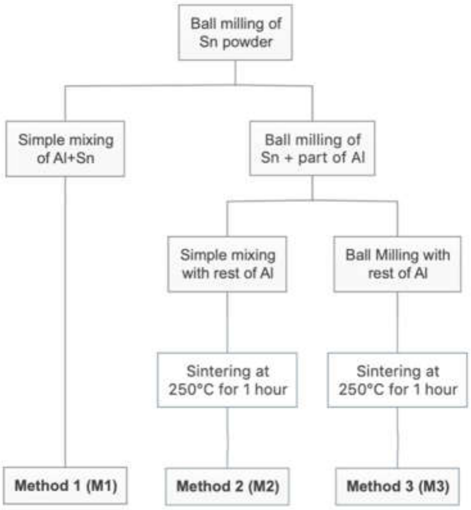

Figure 1. New powder preparation methods

Ball Milling steps were performed in a planetary mill (Retsch PM 400 Planetary Ball Mill), using hardened steel balls of diameter 20 mm (material to ball mass ratio 1:5, about 80% of empty space in the jar) in stainless steel jars. Ethanol was used as lubricant (7% on the total weight of powders), to avoid cold fusion phenomena [12]. To achieve protection from oxidation, the jars were filled with Ar before each process step. Powders were ground at 250 rpm, alternating grinding cycles of 20 minutes to pause cycles of 10 minutes to avoid excessive increases in temperature due to friction and to further minimize oxidation phenomena. For step 1, BM lasted 6 hours, while, the other steps lasted 2 hours each. This process was developed in a previous study about BM PCMs [8]; the only difference is the reduction of single BM time (from 24 hours to 6/2 hours) to avoid too fine microstructures.

From now on, the specimens will be called with the label of their powder preparation method (M1, M2, M3), since further processing is almost the same for all of them.

2.3 Compaction and sintering

Bulk specimens were obtained through cold compression. In facts, according to Gariboldi and Perrin [7], cold compression of Al-Sn powders gives better properties with respect to hot compression, especially in terms of thermal stability. Compression consisted of two steps: force up to 20 kN at 3 mm/min and then force up to 53 kN at 1 mm/min. Finally, cylindrical sample were obtained with diameter 15 mm and height around 20 mm (20.21 mm, 17.76 mm, 21.47 for M1, M2 and M3, respectively). After compaction, M2 and M3 samples were sintered at 250°C for 1 hour, to improve mechanical resistance.

2.4 Characterization

X-Ray Diffraction (XRD) analysis was performed at room temperature to verify which crystalline phases were present in each as-produced bulk sample. A Rigaku Smartlab SE X-ray diffractometer was used, operating at 40kV and 30 mA with Cu Kα source and Bragg-Brentano geometry (θ-θ measurement). Crystalline phases were identified comparing the obtained patterns with references from the Crystallography Open Database [15,16] using Maud software [17].

Microstructural characterization was conducted through Scanning Electron Microscopy (SEM), using a W-SEM (Zeiss Evo 50) detecting Back-Scattered Electrons (BSE). Thanks to the significant Z-contrast between Al and Sn, BSE-SEM micrographs show clearly Al and Sn phases without any etching. Quantitative analysis was conducted using ImageJ software [18], assuming that the volume fraction of a phase is equal to its area fraction, as suggested by Underwood [19]. In this way, porosity was measured for all samples. On the other hand, Sn particles were analysed only for M1 and M3, since it was not possible to do the same for M2 sample due to its peculiar microstructure. An area of about 10 mm^2 (two micrographs corresponding to 5 mm^2) was considered for M1 and M2 samples, while an area of about 0.6 mm^2 (three micrographs corresponding to 0.2 mm^2) was considered for M3 samples; areas of different size were necessary to have enough resolution of pores and particles (Sn in M1, ball milled Sn-rich particles in M3) to be analysed as well as to have enough particles representing the microstructure. Particle features taken into account are total particle Area (in μm^2 and its percentage of the total analysed area) and the best ellipse fitting the particle, represented by Major Axis, Minor Axis and Angle with respect to horizontal direction; generally, in the following, the "particle dimension" will correspond to the Major Axis. Moreover, the two shape descriptors are considered: Circularity and Aspect ratio. Circularity (Equation 1) indicates if the particle contour is round and smooth (value tends to 1) or it has irregularities and/or elongated shape (value tends to 0) [20,21]. Aspect Ratio (Equation 2) is the ratio between the major and minor axis of the fit ellipse [20].

$$Circularity = 4\pi \cdot \frac{[Area]}{[Perimeter]^2}$$

Equation 1. Definition of circularity. Area is the particle area in calibrated scale units and perimeter is the length of the outside boundary of the selection [20]

$$Aspect\ Ratio = \frac{[Major\ Axis]}{[Minor\ Axis]}$$

Equation 2. Aspect ratio of the particle's fitted ellipse [20]

Further, grain orientation in as-produced conditions was analysed through Electron Back Scattered Diffraction (EBSD), using an Oxford Instrument C Nano EBSD detector in a high-resolution Field Emission Gun (FEG) SEM (Zeiss Sigma 500). The test was conducted on M2 sample, since its microstructural features are intermediate between the other two samples, as it will be highlighted in Paragraph 4.1. The test was repeated at low magnification (area 622.90×370.16 μm) and at high magnification (area 28.5×7.78 μm) with step size of 0.832 μm and 0.050 μm, respectively, to obtain a suitable resolution.

Vickers microhardness (HV) measurements gave a preliminary characterization of mechanical properties. A Future-tech FM-700 microhardness tester was used, repeating at least five indentations for every sample, with 4.91 N load on the indenter and dwell time of 15 s. The average size of the indentation (d, i.e. arithmetic mean, in millimetres, of the two diagonal lengths d_1 and d_2 of the indentation) obtained applying this test force (F) was determined from the definition of Vickers hardness according to the standard EN ISO 6507-1:2018 [22].

Thermal properties were determined through Differential Scanning Calorimetry (DSC) tests, using a Setaram TG/DSC Labsys 1600 machine. The goal of these analyses was evaluating the stability of PCM thermal behaviour and amount of energy stored over thermal cycles. Tests were conducted on samples of about 55 mg in alumina crucible under Ar inert atmosphere. Applied thermal history consisted of two consecutive cycles between room temperature and 320°C with a heating/cooling rate of 20°C/min, keeping the maximum temperature for 5 min; between the two cycles, temperature was held at 40°C for 20 min. The stored/released energy was determined measuring the area of the transition peak occurring in correspondence of melting/solidification of Sn in the Heat Flux vs. Time curve; the baseline in correspondence of the peak was interpolated as a polynomial curve choosing the suitable grade to obtain the best fitting [23].

3. Results

3.1 Composition

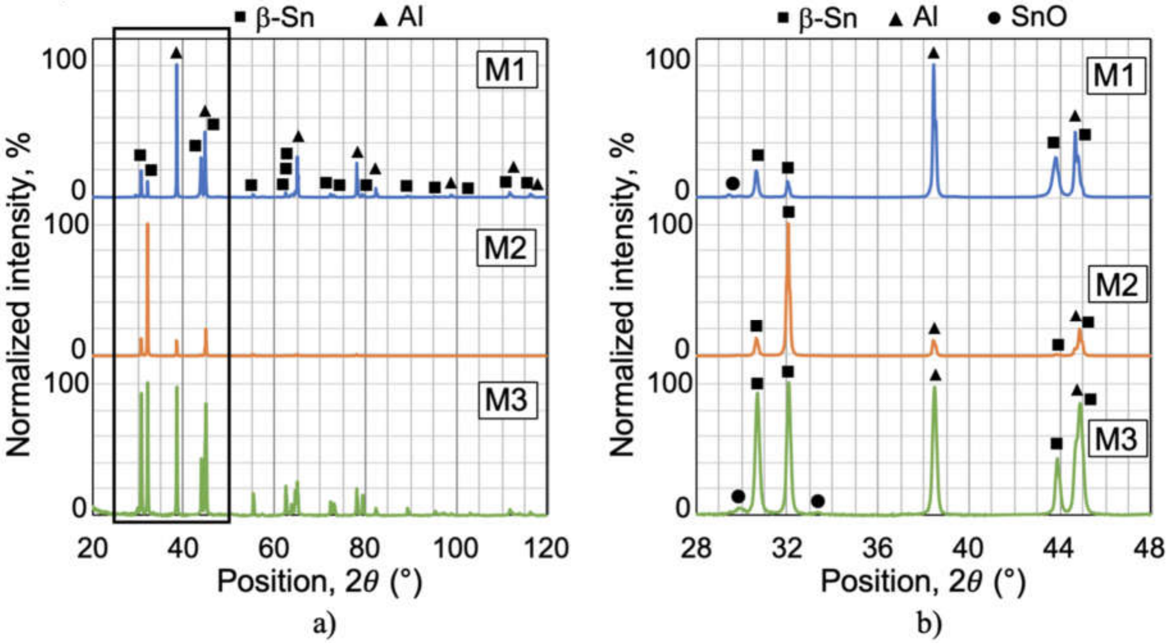

Figure 2. XRD analysis of all samples in as-produced conditions. Intensity is normalized with respect to the maximum value measured in each test. In figure (a), the whole spectrum is showed with indices for Al and Sn only. Figure (b) shows the main peaks at low angles (in the box in figure a), indicating also the traces of SnO.

XRD analysis (Figure 2a) showed that only pure Al and pure β-Sn phases are present in as-produced conditions. Also, small traces of SnO can be observed, however, XRD analysis software (Maud, [17]) considers them significant only in M3 samples.Considering the main Sn peaks at low angles (Figure 2b), their relative intensity changes in different samples. In particular, the first two peaks of both M1 and M3 samples have almost the same height and also the following peaks are in the same range; on the other hand, in sample M2, the peak at 32° is significantly higher than the other Sn peaks.

3.2 Microstructure

Sample produced by Method 1 (BM of Sn powder and SM of this powder with Al) was characterized by coarse microstructure, consisting of a broad distribution of Sn particles, ranging from few microns to more than 400 μm (Figure 3a, Table 3). In BSE-SEM micrographs, the darker phase is Al, whereas the brightest is Sn. Sn particles are generally elongated in direction perpendicular to compression, even if elongation is less evident in smaller particles. In facts, combining results of Fit Ellipse Angle and Aspect Ratio (Table 3), most particles have Aspect Ratio equal or greater than 2, i.e. maximum axis is twice the minimum one, and their angle with respect to horizontal direction is zero, confirming what inferred from image qualitative analysis. After 100 thermal cycles (Figure 3b), both the small, homogeneous particles and the coarse particles of inhomogeneous appearance, are slightly more spherical, but the overall microstructure is pretty similar to the one of as-produced samples.

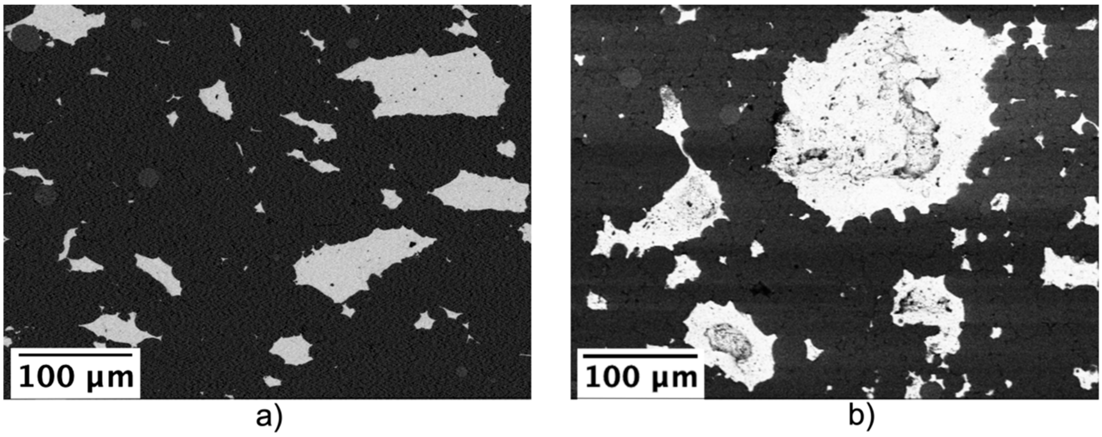

Figure 3. BSE-SEM micrographs of sample obtained by Method 1 (BM of Sn powder and SM of this powder with Al), before thermal cycles (a) and after thermal cycles (b).

The presence of more spherical particles is highlighted also by the increment of average Circularity (mean value from 0.75 to 0.82, as shown in Table 3) and reduction of average Aspect Ratio (mean value from 2.14 to 1.88, Table 3), even if the unvaried mode value suggests that the phenomenon does not occur for all particles, but it is probably more frequent in bigger particles. Sn particles have a concave shape and small black spots are present. According to EDS analysis these black particles consist of Sn (~50%), O and Si; Si impurities were probably present in Al powder. The overall composition of the sample in as-produced conditions from semi-quantitative of BSE-SEM images is Al ~57%m, Sn ~33%m. Concerning porosity content (Figure 4), M1 sample is almost free of pores in as-produced conditions. After thermal cycles porosity content increases to slightly more than 1%.

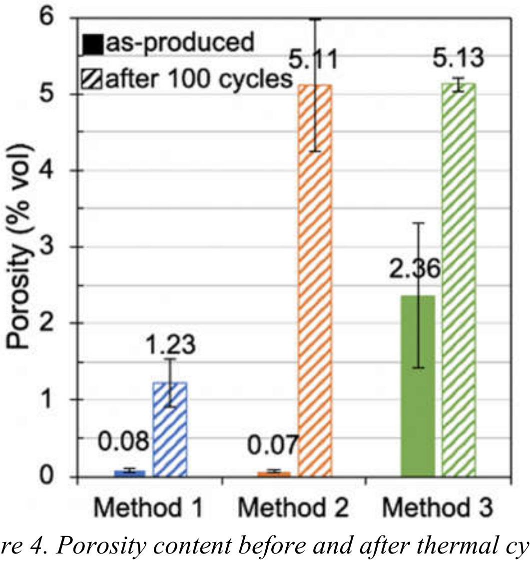

Figure 4. Porosity content before and after thermal cycles

M1	**Area [μm^2, %]**				**Major axis [μm]**		**Minor axis [μm]**		**Angle [°]**		**Circularity**		**Aspect Ratio**	
Cycles	before		after		before	after	before	after	before	after	before	after	before	after
Mean	805.5	0.0081 %	751.5	0.0076 %	31.0	27.3	15.2	15.5	84.0	67.5	0.8	0.8	2.1	1.9
Standard deviation	2609.2	0.0264 %	3197.3	0.0323 %	37.4	31.7	17.2	18.2	67.0	55.8	0.2	0.2	0.9	0.6
Mode	14.5	0.0001 %	34.7	0.0004 %	6.1	9.4	3.0	4.7	0.0	0.0	1.0	1.0	2.0	2.0
Min	14.5	0.0001 %	34.7	0.0004 %	6.1	9.4	2.6	4.0	0.0	0.0	0.1	0.1	1.0	1.0
Max	44067.8	0.4459 %	72256.9	0.7311 %	436.1	458.0	194.5	224.6	180.0	179.9	1.0	1.0	7.5	6.0

Table 3. Results of quantitative analysis on Sn particles in M1 BSE-SEM micrographs; particle Area is reported in μm^2 and percentage with respect to total analysed area (~ 10 mm^2)

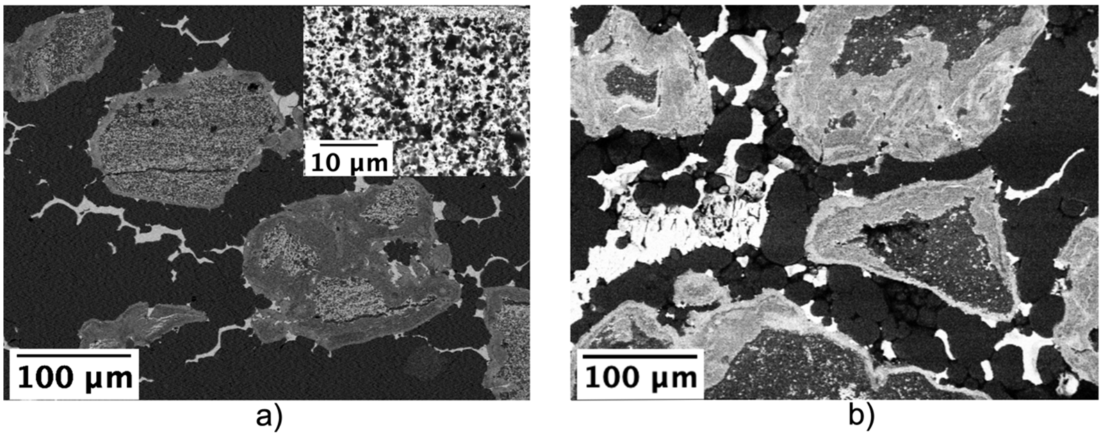

a) b)

Figure 5. BSE-SEM micrographs of sample obtained by Method 2 (BM of Sn powder, BM of this powder with part of Al and SM of this blend with rest of Al), before thermal cycles (a) and after thermal cycles (b); the inset in (a) shows the intermediate Al-Sn area at higher magnification.

In the case of Method 2 (BM of Sn powders, BM of this powder with part of Al, SM with the rest of Al), sintering was performed, and few Sn droplets was observed from outer surfaces. Despite that, the core of the sample is compact, without significative pores (Figure 4). From micrographs, it is possible to observe pure Al, pure Sn and an intermediate, much finer, microstructure consisting of what appear to be a mixture of Al and Sn particles (Figure 5a); high magnification micrograph of Al-Sn mixed region is shown in the inset of Figure 5a. According to EDS, the latter contains around 50-60% mass of Sn in average, while the overall composition in low magnification sample areas is around 30% mass of Sn, with a few percent of O too. Al-Sn regions are contoured by fine Sn-rich grains. After thermal cycles, some leakage on sample surface was observed. Nevertheless, the general features of this microstructure are kept, even if with some differences (Figure 5b). First, in Al-Sn particles, the layer of fine Sn-rich grains becomes thicker and the inhomogeneous Sn distribution suggests its outward diffusion to form the Sn-rich layer. Then, a non-negligible amount of O (~20% mass) is observed in the inner part of coarse Sn particles and it increases up to 24% in their surrounding fine-grain Sn-rich layer (where EDS analyses performed on as-produced sample estimated 15% oxygen). Finally, porosity content increases significantly, as shown in Figure 4.

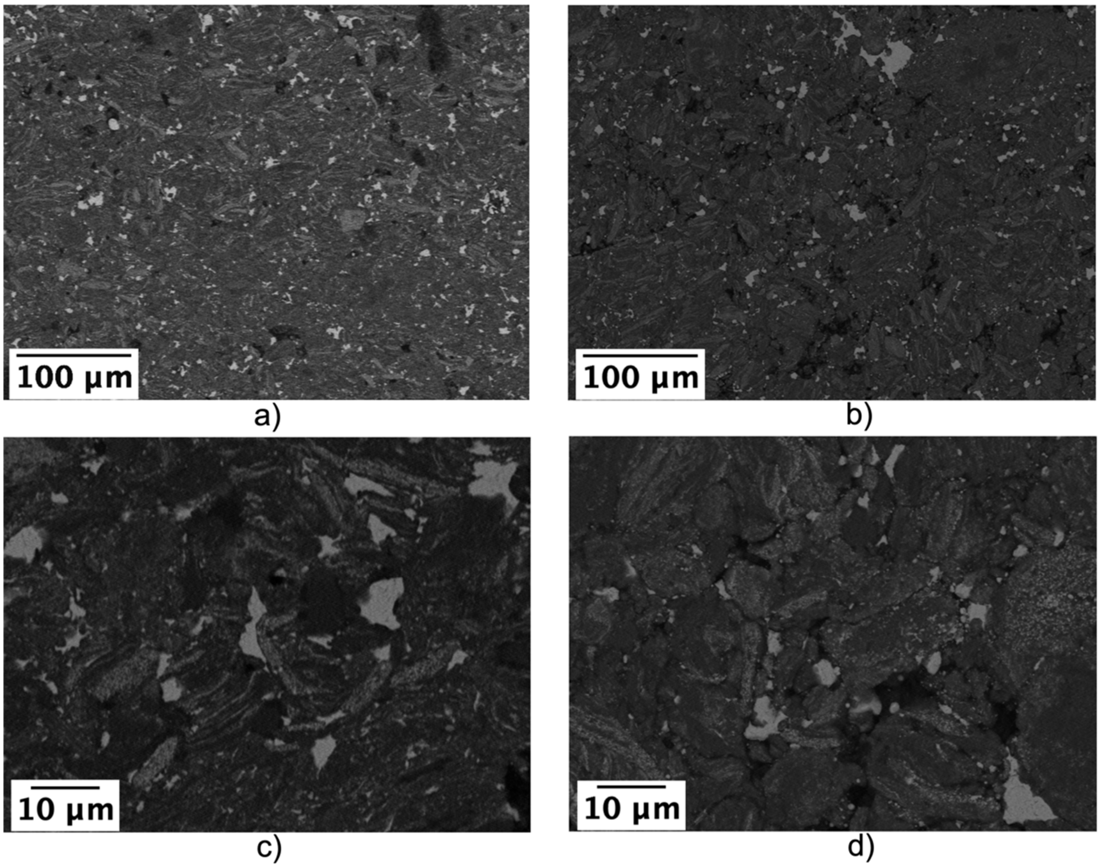

Figure 6. BSE-SEM micrographs of sample obtained by Method 3 (BM of Sn powder, BM of this powder with part of Al and BM of this blend with rest of Al), before (a,c) and after (b,d) thermal cycles at different magnifications.

Sample obtained by Method 3 (BM of Sn powders, BM of this powder with part of Al, BM with the rest of Al) displayed slight tin leakage from outer sample regions during sintering phase. The resulting, as-produced microstructure is the finest (Figure 6a), even if a certain amount of pores (~ 2%) can be observed (Figure 4). They are relatively small (ranging from nanometres or few microns to less than 50 µm) and have a roughly rounded shape in longitudinal sections, suggesting a roughly spherical shape; on the other hand, regions with intermediate composition are elongated perpendicularly to compression direction. According to EDS analysis, the composition is: Al 53.3%m, Sn 33.6%m, O 13.1%m. After 100 thermal cycles, the microstructure, at low (Figure 6b) and at higher magnification (Figure 6d) remains almost the same. However, porosity content increases (Figure 4).

M3	**Area [µm^2, %]**				**Major axis [µm]**		**Minor axis [µm]**		**Angle [°]**		**Circularity**		**Aspect Ratio**	
Cycles	before		after		before	after	before	after	before	after	before	after	before	after
Mean	8.7	0.0015%	9.2	0.0016%	4.1	3.9	1.9	2.1	86.5	84.9	0.6	0.7	2.4	1.9
Standard deviation	20.4	0.0035%	24.1	0.0042%	3.1	2.8	1.4	1.5	62.9	55.8	0.2	0.2	1.2	0.8
Mode	1.4	0.0002%	3.5	0.0006%	1.7	2.6	1.1	1.7	0.0	0.0	1.0	1.0	1.6	1.6
Min	1.4	0.0002%	1.3	0.0002%	1.3	1.3	0.5	0.6	0.0	0.0	0.0	0.1	1.0	1.0
Max	537.6	0.0933%	666.6	0.1157%	44.7	43.3	18.5	25.1	180.0	180.0	1.0	1.0	12.0	9.4

Table 4. Results of quantitative analysis of Sn particles in M3 SEM micrographs; particle Area is reported in µm^2 and percentage with respect to total analysed area (~ 0.6 mm^2)

In the case of M3 sample, quantitative analyses could not include all Sn-rich particles, since sub-micrometric particles have too low resolution to be clearly identified, as shown in high magnification micrograph (Figure 6c). As for M1 specimen, Angle mode equal to zero, increase of mean Circularity and Aspect Ratio prove the tendency of particles to become more spherical, even if it probably more due to evolution of bigger particles, since mode values are still the same (Table 4). Considering Area, Major axis and Minor axis (Table 4), it is possible to suppose that particles tend to become not only more spherical, but also slightly bigger.

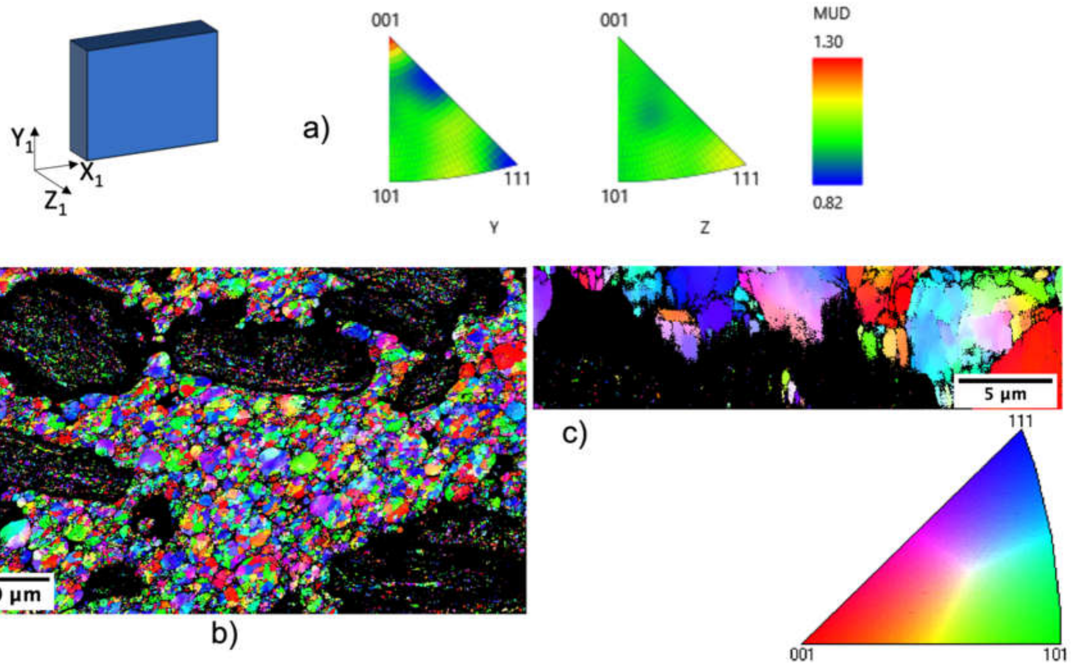

Figure 7. EBSD results for Al phase. In the sample reference system, Y_1 axis is parallel to compression direction and Z_1 is perpendicular to sample surface. a) Inverse Polar Figures (IPFs) with respect to Y_1 and Z_1 axes, expressed in terms of Multiples of Uniform Density (MUD). b) IPF Map with respect to Y_1 axis at low magnification. c) IPF map with respect to Y_1 axis at high magnification, including a Sn coarse particle and the boundary of an Al-Sn region.

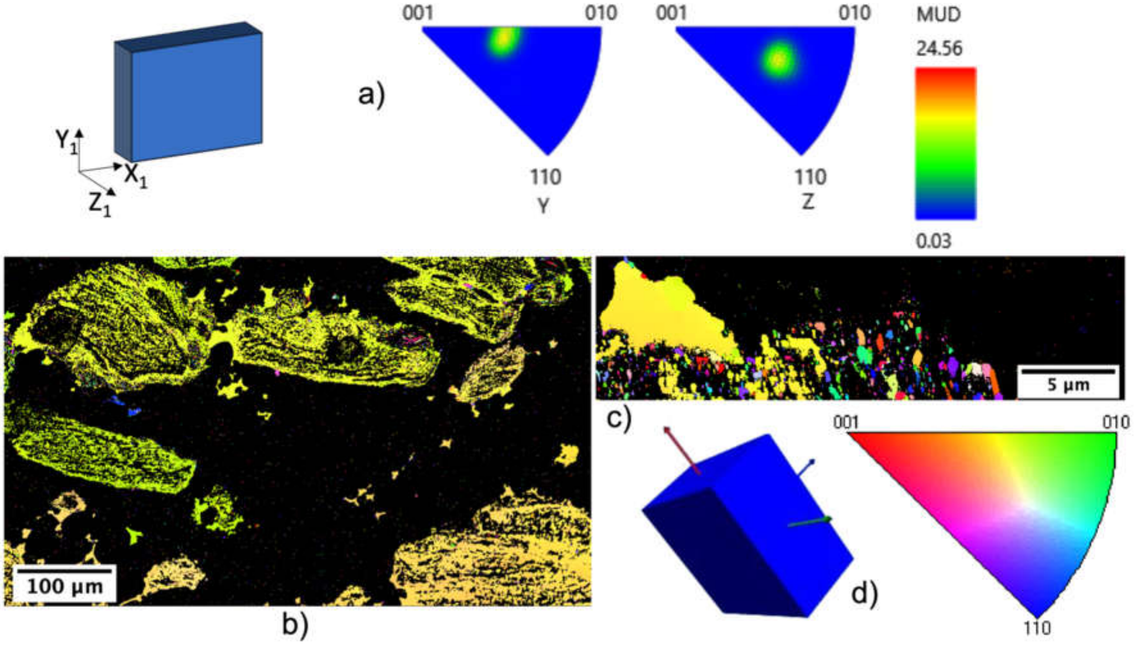

Figure 8. EBSD results for Sn phase. In the sample reference system, Y_1 axis is parallel to compression direction and Z_1 is perpendicular to sample surface. a) Inverse Polar Figures (IPFs) with respect to Y_1 and Z_1 axes, expressed in terms of Multiples of Uniform Density (MUD). b) IPF Map with respect to Y_1 axis at low magnification. c) IPF map with respect to Y_1 axis at high magnification, including a Sn coarse particle and the boundary of an Al-Sn region. d) Sn unit cell oriented as in the sample.

EBSD Inverse Polar Figures (IPFs) and IPF maps for Al phase are presented in Figure 7. According to both the IPFs (Figure 7a) and the IPF maps (Figure 7b-c), orientations of Al grains are randomly distributed. This observation is valid in the core of the phase as well on the boundaries, where Al is in contact with Sn. On the other hand, the two IPFs of Sn (Figure 8a) show that the most of Sn crystallographic poles are oriented in the same direction, which is highlighted also in the IPF maps (Figure 8b-c), where the most of Sn area has the same colour with little tone variations. This homogeneous orientation is particularly evident along Y_1 axis.

3.3 Mechanical properties

Results of Vickers Microhardness tests are summarized in Figure 9. Hardness of M1 and M2 samples is around 40 HV before thermal cycles and then decreases to 35 HV on average. Considering the higher standard deviation after cycles, the reduction is even less significant. M3 sample show a higher hardness (~54 HV), which is almost constant after cycles. Indentation diagonal size and area of corresponding indentations, computed according to standards [22], are reported in Table 5. Comparing these values with mean size and area of Sn particles, it is evident that indentations are significantly bigger than regions inside the material. Therefore, each hardness measurement generally depends on more than one phase.

	Mean HV	**Standard deviation**	**Corresponding indentation size [μm]**	**Corresponding indentation area [μm^2]**	**Mean size of Sn particles* [μm]**	**Mean area of Sn particles [μm^2]**
M1	42.42	1.25	147.83	10926.45	30.99	805.50
	33.98	3.70	165.17	13640.38	27.25	751.47
M2**	41.18	1.54	150.04	11255.46	66.38	4286.18
	36.48	7.06	159.41	12705.59	68.56	5432.93
M3	54.40	2.53	130.54	8520.22	4.12	8.71
	54.18	5.91	130.80	8554.82	3.90	9.17

**Major Axis of the Fit Ellipse*

***for M2 sample, the considered particles are both Sn particles and Al-Sn regions*

Table 5. Comparison of indentation size and area corresponding to mean value of Vickers microhardness with Sn particles size and area.

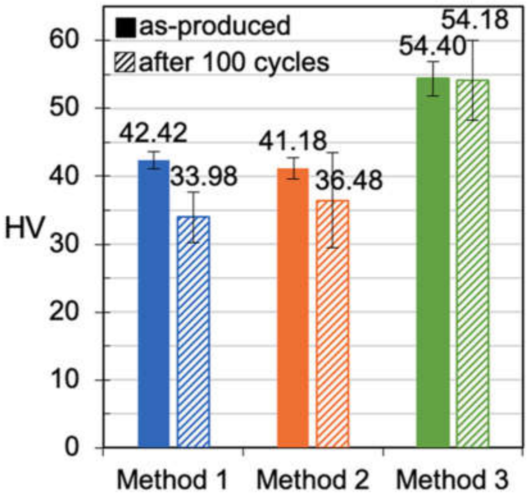

Figure 9. Results of Vickers Microhardness tests before and after thermal cycles

3.4 Thermal response

Melting peaks in DSC curves are shown in Figure 10-a for each sample before and after thermal cycles. The peak has a V-shape and its onset temperature can be assumed around 227°C, even if for

M2 and M3 the peak onset is very smooth and difficult to identify the exact value. The V-shape is kept after thermal cycles, but the peak tends to move at lower temperatures and its height decreases. M3 sample shows the less significant changes with respect to the other samples. On the other hand, solidification gives rise to multiple broad peaks. M1 sample has two peaks between 170°C and 230°C, which appear also after thermal cycles; almost no undercooling occurs in the first thermal cycles, while after 100 cycles an undercooling of ~10°C is observed. Considering M3 samples, it is difficult to define the onset of transition; however, solidification clearly begins at temperatures lower than 180°C and ends at around 80°C. After 100 thermal cycles, the situation is generally unvaried, even if a short and broad peak form around 180°C. The curve of M2 sample can be considered as an "intermediate" situation with respect to the other two: it has both broad short peaks at low temperatures (below 180°C) and taller peaks between 180°C and 225°C.

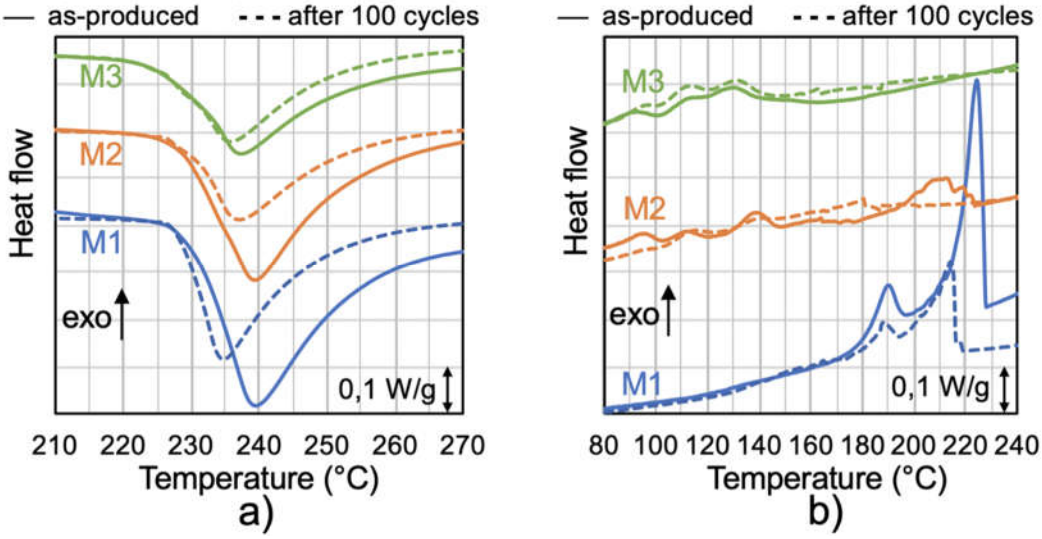

Figure 10. Melting (a) and solidification (b) peaks in DSC curves for as-produced and cycled samples.

Transition enthalpies determined from DSC curves are shown in Figure 11. Due to the complex shape of the solidification peak, only melting peaks were considered in the calculation. In as-produced conditions, the highest value is observed for M1 sample (19.28 J/g), the lowest for M3 sample (11.56 J/g). After thermal cycles, reduction of transition enthalpy is observed for every sample: ~38% for M1, ~48% for M2 and ~25% for M3.

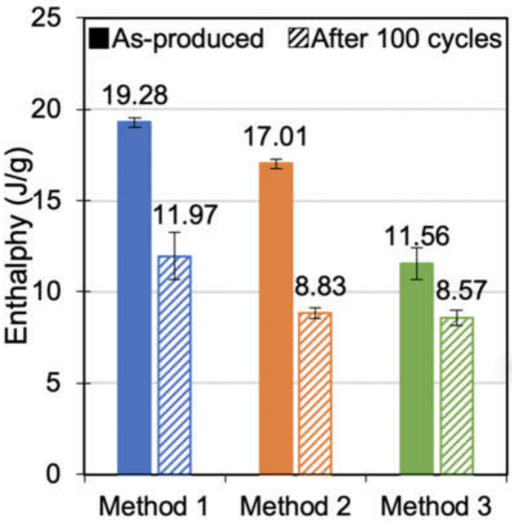

Figure 11. Melting enthalpy before and after thermal cycles

4. Discussion

4.1 Composition

The applied powder metallurgy process gave Al-Sn alloy almost without formation of other phases or contaminations. The exception is the formation of SnO, reasonably related to ball milling process; in facts, the longer is the ball milling process (one, two or three steps), the more oxide is formed. Despite the protective Ar atmosphere, contamination occurred. Suryanarayana reported that this is a critical and complex issue to be solved, because, even flushing inert gas in the container, some oxygen could not be removed from internal surfaces where it is absorbed [14]. However, the use of Ar atmosphere is recommended to mitigate this issue [14]. Therefore, a further process optimization could involve a better control of the environment in the jar during ball milling, e.g. using longer time to achieve vacuum before adding inert gas and/or using other gas atmospheres. Moreover, it could be interesting also to consider different time processes.

4.2 Microstructure: were the targets hit?

4.2.1 Method 1

The main aim of M1 was to obtain compact Sn particles, i.e. with high circularity and low aspect ratio. This should prevent them flowing among Al grains during compression and, in the end, the final microstructure should avoid leakage. As highlighted by both qualitative and quantitative analysis of BSE-SEM micrographs, Sn particles in M1 sample have generally a relatively rounded shape and are well isolated inside the Al matrix. This result confirms a positive effect of ball milling of Sn powder to reduce the difference of hardness with Al powder, since Sn particles are not flattened too much during compression. Moreover, Sn particles became more circular after thermal cycles, therefore a sintering heat treatment could be useful to obtain this feature also in as-produced samples. In addition to the suitable Sn particle shape and distribution, this method results in a dense material, almost without porosity in as-produced conditions and significantly lower content with respect to the other two methods after thermal cycles.

4.2.2 Method 3

M3 gave a microstructure close to the desired one: very fine with good isolation of Sn particles. Nevertheless, non-negligible amount of porosity is observed. Despite of that, this microstructure is quite stable with respect to those obtained through M1 and M2 and probably higher compression stresses could have led to even less porosity and higher microstructural stability.

4.2.3 Method 2

The goal of M2 was to obtain an intermediate microstructure between the coarse one of M1 and the fine one of M3. In practice, the second ball milling step formed generally isolated regions containing an extremely fine distribution of Al and Sn, like in M3 sample microstructure, which have a Sn-rich external layer. In addition, like in M1 sample, coarse Sn particles are observed. The difference is that the latter form elongated and interconnected particles, from which Sn tends to leak toward the surface; in facts, shape and position of pores after cycles (i.e. around Al grains) correspond to shape and position of coarse Sn particles before cycles. Microstructure obtained through this method is not stable as expected, due to Sn leakage as well as the motion of Sn from the inner part of Al-Sn regions towards their boundaries.

Further, EBSD analysis of this sample shows a preferential grain orientation of Sn in longitudinal direction, which corresponds to the main heat flow direction during cooling after sintering. Actually, samples were simply cooled down in air and, so, the most of heat flux was reasonably removed perpendicularly to the metallic substrate where the sample was on, i.e. along the axis of the cylindrical specimen. Moreover, it is not possible to identify a relationship between Al grains and Sn particles, because Sn has a preferential orientation everywhere and Al grains in contact with it are randomly oriented. As reported by Ma et al. [24], the anisotropy of Sn could affect thermal expansion and mechanical properties. However, in the tests performed up to now, clear effects of this feature were not observed. Nevertheless, it will be considered in the analysis of further mechanical tests.

4.3 Hardness

Microhardness values of M1 and M2 samples (~40 HV) as well as the one of M3 sample (~54 HV) are higher than the ones of cast Al-Sn alloys, which are usually around 30 HV [12]. This effect is ascribed to powder hardening during ball milling; however, thermal cycles are likely to cause relaxation and recrystallization of the alloy, which explains the reduction of hardness for M1 and M2. Conversely, M3 sample keeps its high hardness level also after thermal cycles. The explanation of this behaviour can be found considering a different hardening mechanism, i.e. precipitation hardening. Liu et al. [25] studied the correlation of Sn distribution on hardness in a nanostructured Al-Sn alloy obtained by powder metallurgy (ball milling, cold compression and sintering). They demonstrated that a homogeneous distribution of soft Sn in Al matrix improves the hardness of the alloy through dispersion hardening [25]. It is reasonable to assume that, [25] despite the higher amount of tin in the present case, the same mechanism occurs in M3 sample since it has an extremely fine microstructure, which is similar to the ones presented by Liu et al. Moreover, this mechanism is not related to hardening of powders, which is reduced during thermal cycles due to relaxation, but to the fine microstructure, which is stable even after many cycles. Therefore, this interpretation can explain hardness stability after simulated service. Higher content of pores in as produced M3 sample and in all cycled samples causes more scattering in standard deviation.

4.4 Thermal response

4.4.1 Stored energy

All the samples have a DSC-measured melting enthalpy lower than the theoretical value computed for a Al-40%m Sn alloy, i.e. 23.6 J/g. Considering M1 sample in as-produced conditions, the energy value (19.28 J/g) is quite close to the one that can be obtained using the effective composition determined through semi-quantitative measurements (i.e. ~33%m Sn, 19.47 J/g). After thermal cycles, measured enthalpy is even lower because some Sn leakage occurred, as demonstrated by visual analysis of sample surfaces just after simulated service and by the increment of porosity in correspondence of former coarse Sn particles (Paragraph 4.1.3). On the other hand, M3 sample shows a significantly lower melting enthalpy, despite a measured composition close to the nominal one. Authors think that this behaviour is related to the extremely fine microstructure which is characterized by micrometric and sub-micrometric Sn particles, but the actual mechanism is still not completely clear. However, despite the low energy amount, M3 sample gives the most stable thermal response. Finally, M2 sample, consisting of both coarse and fine Sn particles, behaves mainly as M1 sample; however, the reduction of stored energy with respect to the nominal one, especially after thermal cycles, could be also affected by the presence of the intermediate Al-Sn region containing fine Sn particles.

4.4.2 Thermal response mode

Analysis of transition peak shape in DSC curves allows to evaluate the “thermal response mode” of the material. Considering melting peaks (Figure 10a), they have always a V-shape and the width is generally the same for all the processes. Therefore, it is possible to conclude that melting behaviour is independent of microstructure and, consequently, it is independent of production process. The temperature that is assumed as activation temperature is lower than pure Sn melting temperature, but close to eutectic temperature. It is possible to ascribe this behaviour partially to the occurrence of eutectic reaction, but also to the presence of small particles which can lower the melting temperature with respect to bulk Sn. Also, the experimental error related to DSC machine calibration should be considered. Nevertheless, considering the final application of this material, these small differences are still acceptable. After thermal cycles, melting peaks are shorter and narrower, due to leakage of Sn during thermal cycles; in facts, this is more evident for M1 and M2 samples, which experienced more Sn losses.

On the other hand, solidification peaks change significantly in different production processes (Figure 10b). According to Kim and Cantor [26], solidification of Sn droplets in a solid Al matrix can occur at different temperatures below Sn melting temperature depending on their size; in particular, smaller particles solidify at lower temperature, showing a higher undercooling. These authors ascribe this behaviour to the lower probability to find in smaller Sn droplets trace impurities that can act as nucleation catalysts, increasing the undercooling necessary to their solidification [26]. In the case of the present study, since some Sn particles are even smaller than in the case of Kim and Cantor [26], also some effect due to nanometric size can contribute to increase undercooling [27].

Based on these concepts, solidification peaks observed in the present study can be reasonably correlated to the relative sample microstructures. M1 sample, which has the coarser microstructure, has two high peaks with onset between 220°C and 230°C, i.e. with a low undercooling (less than 10°C); this behaviour occurs both before and after thermal cycles simulating service. Instead, in M3 sample, which has an extremely fine microstructure, solidification starts at significantly lower temperatures (below 180°C) and takes wider temperature ranges (about 80°C with respect to about 50°C of the M1 case). Finally, M2 sample has a microstructure that can be considered as intermediate between M1 and M3 samples with both coarse and fine microstructure in Al-Sn regions and, consequently, also its thermal response is intermediate between the other two, having both peaks close to transition temperature and with an undercooling of more than 60÷70°C.

Moreover, the formation or growth of peaks at intermediate temperatures (160°C÷180°C) in M3 and, especially, in M2 can be related to the coarsening of smaller particles noticed in micrographs. In conclusion, it is evident that solidification behaviour is strongly dependent on the microstructure and, so, on the production method: increasing the number of ball-milling steps, the final microstructure will result finer and consequently the thermal response will be shifted towards lower temperatures. This implies that thermal response of the material could be tailored according to the application requirements, i.e. fast or smooth heat release. For example, a slow heat release could be useful in mechanical components to reduce thermal stresses during heat release.

5. Conclusions

1) Ball milling of Sn powder before mixing with Al is effective to reduce the hardness difference between the two metals. In this way, Sn particles are more rounded and less interconnected, reducing leakage and improving thermal stability.
2) Mixing of Al and Sn powder through ball milling allows to obtain a fine microstructure with better mechanical properties with respect to simple mixing. Further, particle size dependent undercooling was revealed. Nevertheless, some collateral drawbacks were observed: a higher oxygen content and stored energy lower than expected for the actual Sn content.
3) Observations on Method 2 combining SM and BM confirmed that microstructure has a strong effect on thermal response, especially on cooling. Therefore, it is potentially possible to design the microstructure to obtain the desired response in cooling, i.e. fast or slow heat release.

Acknowledgements

The Authors would like to thank Andrea Maggi and Fabio Falgari for their help in thermal characterization, and Filippo Belelli, for his help in XRD tests.

This work was supported by the Italian Ministry for Education, University and Research through the project Department of Excellence LIS4.0 (Integrated Laboratory for Lightweight e Smart Structures).

Author contributions

Chiara Confalonieri: Investigation, Formal analysis, Writing – Original Draft, Writing – Review and Editing. Maxime Perrin: Investigation, Formal analysis, Writing – Review and Editing. Elisabetta Gariboldi: Conceptualization, Methodology, Investigation, Writing – Review and Editing.

Declarations of interest

None.

Data availability

The raw data required to reproduce these findings cannot be shared at this time as the data also forms part of an ongoing study. The processed data required to reproduce these findings cannot be shared at this time as the data also forms part of an ongoing study.

References

[1] K. Pielichowska, K. Pielichowski, Phase change materials for thermal energy storage, Prog. Mater. Sci. 65 (2014) 67–123. doi:10.1016/J.PMATSCI.2014.03.005.

[2] W. Su, J. Darkwa, G. Kokogiannakis, Review of solid–liquid phase change materials and their encapsulation technologies, Renew. Sustain. Energy Rev. 48 (2015) 373–391. doi:https://doi.org/10.1016/j.rser.2015.04.044.

[3] A. Safari, R. Saidur, F.A. Sulaiman, Y. Xu, J. Dong, A review on supercooling of Phase Change Materials in thermal energy storage systems, Renew. Sustain. Energy Rev. 70 (2017) 905–919. doi:https://doi.org/10.1016/j.rser.2016.11.272.

[4] C. Zhou, S. Wu, Medium- and high-temperature latent heat thermal energy storage: Material database, system review, and corrosivity assessment, Int. J. Energy Res. 43 (2019) 621–661. doi:10.1002/er.4216.

[5] A.I. Fernández, C. Barreneche, M. Belusko, M. Segarra, F. Bruno, L.F. Cabeza, Considerations for the use of metal alloys as phase change materials for high temperature applications, Sol. Energy Mater. Sol. Cells. 171 (2017) 275–281. doi:https://doi.org/10.1016/j.solmat.2017.06.054.

[6] H. Sugo, E. Kisi, D. Cuskelly, Miscibility gap alloys with inverse microstructures and high thermal conductivity for high energy density thermal storage applications, Appl. Therm. Eng. 51 (2013) 1345–1350. doi:10.1016/J.APPLTHERMALENG.2012.11.029.

[7] E. Gariboldi, M. Perrin, Metallic Composites as Form-Stable Phase Change Alloys, in: THERMEC 2018, Trans Tech Publications, 2019: pp. 1966–1971. doi:10.4028/www.scientific.net/MSF.941.1966.

[8] C. Confalonieri, Z. Li, E. Gariboldi, Metallic Form-Stable Phase Change Materials for Thermal Energy Storage and Management: general features and effect of manufacturing process on thermal response and stability, La Metall. Ital. - Int. J. Ital. Assoc. Metall. 7/8 (2019) 12–20.

[9] A.J. McAlister, D.J. Kahan, The Al−Sn (Aluminum-Tin) System, Bull. Alloy Phase Diagrams. 4 (1983) 410–414. doi:10.1007/BF02868095.

[10] O.A. Chikova, A.N. Konstantinov, E. V Shishkina, D.S. Chezganov, Nanoindentation study of the effect of the structural state of the melt on the crystal structure and mechanical properties of the phases in an Al-50 wt % Sn alloy, Russ. Metall. 2013 (2013) 535–544. doi:10.1134/S0036029513070045.

[11] T. Stuczyñski, Metallurgical problems associated with the production of aluminium-tin alloys, Mater. Des. 18 (1997) 369–372. doi:https://doi.org/10.1016/S0261-3069(97)00078-2.

[12] X. Liu, M.Q. Zeng, Y. Ma, M. Zhu, Promoting the high load-carrying capability of Al–20wt%Sn bearing alloys through creating nanocomposite structure by mechanical alloying,

Wear. 294–295 (2012) 387–394. doi:10.1016/j.wear.2012.07.021.

[13] L. Balanović, D. Živković, D. Manasijević, D. Minić, B. Marjanović, Calorimetric study and thermal analysis of Al–Sn system, J. Therm. Anal. Calorim. 111 (2013) 1431–1435. doi:10.1007/s10973-012-2499-8.

[14] C. Suryanarayana, Mechanical alloying and milling, Prog. Mater. Sci. 46 (2001) 1–184. doi:https://doi.org/10.1016/S0079-6425(99)00010-9.

[15] S. Gražulis, A. Daškevič, A. Merkys, D. Chateigner, L. Lutterotti, M. Quirós, N.R. Serebryanaya, P. Moeck, R.T. Downs, A. Le Bail, Crystallography Open Database (COD): an open-access collection of crystal structures and platform for world-wide collaboration, Nucleic Acids Res. 40 (2012) D420–D427. doi:10.1093/nar/gkr900.

[16] R.W.G. Wyckoff, Second edition. Interscience Publishers, New York, Cryst. Struct. 1 (1963) 7–237.

[17] L. Lutterotti, Maud, (n.d.). http://maud.radiographema.eu.

[18] W.S. Rasband, ImageJ, (2018). https://imagej.net/Welcome.

[19] E. Underwood, The Mathematical Foundations of Quantitative Stereology, in: G. Pellissier, S. Purdy (Eds.), Stereol. Quant. Metallogr., ASTM International, West Conshohocken, PA, 1972: pp. 3–38. doi:10.1520/STP36841S.

[20] T. Ferreira, W. Rasband, ImageJ User Guide, (2012). https://imagej.nih.gov/ij/docs/guide/146.html (accessed November 25, 2019).

[21] Y. Takashimizu, M. Iiyoshi, New parameter of roundness R: circularity corrected by aspect ratio, Prog. Earth Planet. Sci. 3 (2016) 2. doi:10.1186/s40645-015-0078-x.

[22] EN ISO 6507-1:2018, Metallic materials – Vickers hardness test, Part 1: Test method, (2018) 30.

[23] W.F. Hemminger, S.M. Sarge, The baseline construction and its influence on the measurement of heat with differential scanning calorimeters, J. Therm. Anal. 37 (1991) 1455–1477. doi:10.1007/BF01913481.

[24] Z.L. Ma, H. Shang, A.A. Daszki, S.A. Belyakov, C.M. Gourlay, Mechanisms of beta-Sn nucleation and microstructure evolution in Sn-Ag-Cu solders containing titanium, J. Alloys Compd. 777 (2019) 1357–1366. doi:https://doi.org/10.1016/j.jallcom.2018.11.097.

[25] X. Liu, M.Q. Zeng, Y. Ma, M. Zhu, Melting behavior and the correlation of Sn distribution on hardness in a nanostructured Al–Sn alloy, Mater. Sci. Eng. A. 506 (2009) 1–7. doi:10.1016/J.MSEA.2008.12.054.

[26] W.T. Kim, B. Cantor, Solidification of tin droplets embedded in an aluminium matrix, J. Mater. Sci. 26 (1991) 2868–2878. doi:10.1007/BF01124815.

[27] B. Yang, Y. Gao, C. Zou, Q. Zhai, E. Zhuravlev, C. Schick, Size-dependent undercooling of pure Sn by single particle DSC measurements, Chinese Sci. Bull. 55 (2010) 2063–2065. doi:10.1007/s11434-010-3041-7.